Valley physics and anomalous valley Hall effect in single-layer *h-M*NX (*M* = Ti, Zr, Hf; *X* = Cl, Br)

Pei Zhao,[1] Yan Liang,[1,*] Yandong Ma,[2,†] and Thomas Frauenheim[3]

[1]*Department of Physics, College of Information Science and Engineering, Ocean University of China, Qingdao 266100, China*
[2]*School of Physics, State Key Laboratory of Crystal Materials, Shandong University, Shandanan Street 27,*
Jinan 250100, People's Republic of China
[3]*Bremen Center for Computational Materials Science, Universität Bremen, Am Fallturm 1, 28359 Bremen, Germany;*
Beijing Computational Science Research Center, Beijing 100193, China;
and Shenzhen JL Computational Science and Applied Research Institute, Shenzhen 518109, China

Recently, the valley degree of freedom of electrons in two-dimensional materials has been attracting growing attention as an information carrier. Here, on the basis of first-principles calculations, we propose a series of unique 2D valleytronic materials in single-layer *h-M*NX (*M* = Ti, Zr; Hf, *X* = Cl, Br) and systematically investigate their valleytronic properties. The underlying valley-contrasting physics including valley spin splitting and valley-dependent optical selection rules in single-layer *h-M*NX is unveiled. Moreover, we find that the intriguing valley polarization in single-layer *h-M*NX can be achieved through both circularly polarized light and a ferromagnetic substrate. The substrate-induced valley polarization in SL *h-M*NX is stacking dependent and can be enhanced by decreasing the interlayer distance. Our findings thus provide a tantalizing platform for operating the valley index in two-dimensional materials.

I. INTRODUCTION

In addition to charge and spin, the valley index, characterizing the energy extreme of band structure, is rapidly emerging as a distinctive electronic degree of freedom of electrons, which has simulated intensive research interest recently [1–3]. Once breaking structural inversion symmetry, the carriers in inequivalent valleys are subjected to valley-contrasting physical quantities, such as the Berry curvature and orbital magnetic moments, making the generation, manipulation, and detection of the valley index accessible. Analogous to charge for electronics and spin for spintronics, manipulating and utilizing the valley index as an information carrier to store information and perform logic operations can lead to the parallel concept of valleytronics [4,5]. Especially in two-dimensional (2D) materials with valleys locating at the $+K$ and $-K$ points, due to the large separation in the momentum space, the valley index is robust against scatterings resulting from deformation and long-wavelength phonons. Therefore, compared with conventional valleytronic materials, 2D valleytronic materials hold great promise for developing high-performance valleytronic devices [6–9].

The first proposal for realizing 2D valleytronics is suggested in graphene; however, due to the centrosymmetric structure and weak spin-orbital coupling (SOC), its practical valleytronic applications are extremely limited [10,11]. Different from graphene, the inversion symmetry in 2D transition metal dichalcogenides (TMDs) is broken naturally. This,

combined with strong SOC, makes 2D TMDs the most qualified candidates in the valleytronics field [12–17]. To utilize the valley index, it is necessary to produce the valley polarized state. In TMDs, time-reversal symmetry restricts the spin at the $+K$ and $-K$ valleys to be opposite but energetically degenerate, giving rise to the valley-contrasting optical selection rules. Accordingly, dynamical valley polarization has been experimentally realized in 2D TMDs through circularly polarized optical pumping [18–20]. An alternative avenue to realize valley polarization in 2D TMDs is to break the time-reversal symmetry. By applying an external magnetic field, atom doping, or magnetic proximity effect [21–27], the valley degeneracy can be lifted due to the broken time-reversal symmetry, rendering populating one of the valleys accessible. In addition, spin-valley locking enables long valley lifetimes of TMD monolayers and their heterostructures [28,29], which opens up new opportunities for the applications in spintronics [30]. Although much effort has been devoted to 2D valleytronics [31–33], the understanding of valley spin splitting remains to be developed, and research on transport properties of valley materials under light irradiation is still rare; both of these limit further development and applications in valleytronic devices.

In this work, using first-principles calculations, we propose a series of unique 2D valleytronic materials in single-layer (SL) *h-M*NX (*M* = Ti, Zr, Hf; *X* = Cl, Br). Our results show that SL *h-M*NX is a semiconductor with a moderate band gap locating at the $+K$ and $-K$ points, forming two inequivalent valleys. Upon taking SOC into consideration, the valleys of SL *h-M*NX exhibit a large valley spin splitting. Interestingly, the large valley spin splitting occurs at the conduction band minimum (CBM) rather than the valence band maximum

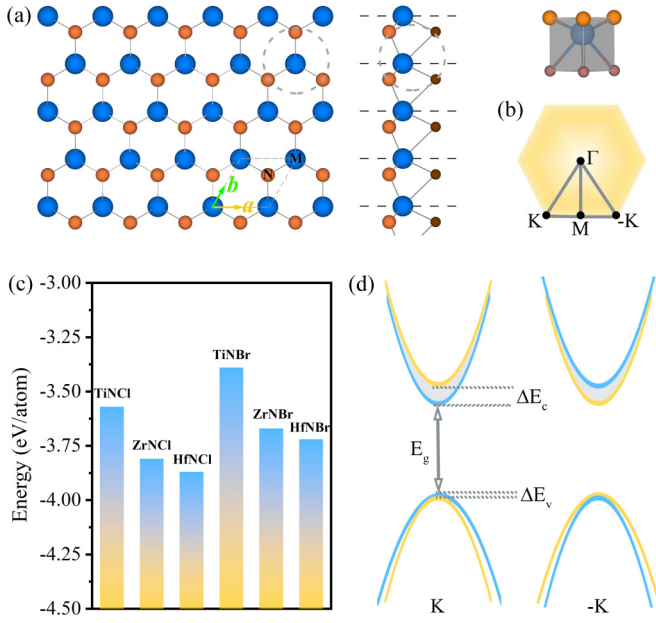*yliang.phy@ouc.edu.cn
†yandong.ma@sdu.edu.cn

FIG. 1. (a) Top and side views of the crystal structure of SL h-MNX. Inset in (a) displays the distorted trigonal prismatic geometry. Blue, orange, and brown balls represent M, N, and X atoms, respectively. (b) 2D Brillouin zone (BZ); the high-symmetry points are marked. (c) The calculated formation energies of SL h-MNX. (d) Schematic of the band edges around the +K and −K points. Yellow and blue lines in (d) are spin-up and spin-down states, respectively.

TABLE I. The optimized lattice constants (a), band gaps (E_g), spin splitting of VBM (ΔE_v) and CBM (ΔE_c), and Berry curvature (Ω) at the K point for SL h-MNX.

	a(Å)	E_g(eV)	ΔE_v(meV)	ΔE_c(meV)	Ω (bohr^2)
TiNCl	3.13	1.60	5	38	10.0
ZrNCl	3.36	2.16	4	50	12.0
HfNCl	3.32	2.39	14	142	7.5
TiNBr	3.21	1.31	6	55	10.4
ZrNBr	3.43	1.96	6	73	10.3
HfNBr	3.38	2.16	19	162	7.2

reaction, which can demonstrate their experimental feasibility. To further examine the stability of SL h-MNX, the phonon dispersion relations are also calculated. From Fig. S1 in the Supplemental Material [34] (also see Refs. [35–49]), we find that there is no image frequency in the whole Brillouin zone (BZ), indicating the dynamical stability.

The band structures of SL h-MNX without SOC based on the HSE06 functional are shown in Figs. 2(a), and S2 in the Supplemental Material [34]. Clearly, all these systems are semiconductors with a direct band gap locating at the +K and −K points. Therefore, all these systems are 2D valleytronic materials with two valleys at the +K and −K points. Upon introducing SOC, due to the noncentrosymmetric structures of

(VBM), which is different from that of the typical 2D valleytronic materials. Our calculations for photocurrent further suggest that circularly polarized light can produce valley polarization in these systems. Moreover, taking SL h-HfNCl as an example, we construct HfNCl/CrBr$_3$ van der Waals (vdW) heterostructures, and find that the valley polarization in these systems can also be achieved through magnetic proximity effect. The corresponding physical mechanisms are discussed in detail. All these interesting properties make SL h-MNX appealing for potential applications in 2D valleytronic devices.

II. RESULTS AND DISCUSSION

Figure 1(a) shows the crystal structures of SL h-MNX. It can be seen that SL h-MNX exhibits a hexagonal lattice with the space group C_{3v}. Its unit cell consists of three atoms called M, N, and X, with the M atomic layer sandwiched between the N and X atomic layers. Each M atom is coordinated by three N atoms and three X atoms, forming a distorted trigonal prismatic geometry. The details about the lattice parameters of SL h-MNX are summarized in Table I. The formation energies of SL h-MNX are estimated based on the following equation:

$$E_f = (E_{\text{total}} - E_M - E_N - E_X)/3.$$

Here, E_{total} is the energy of the unit cell of SL h-MNX. E_M, E_N, and E_X are the chemical potentials of the M, N, and X atoms, respectively, which are calculated from their corresponding elemental bulk phases. As shown in Fig. 1(c), the obtained formation energies are much less than 0 eV, indicating the synthesized process is a spontaneous exothermic
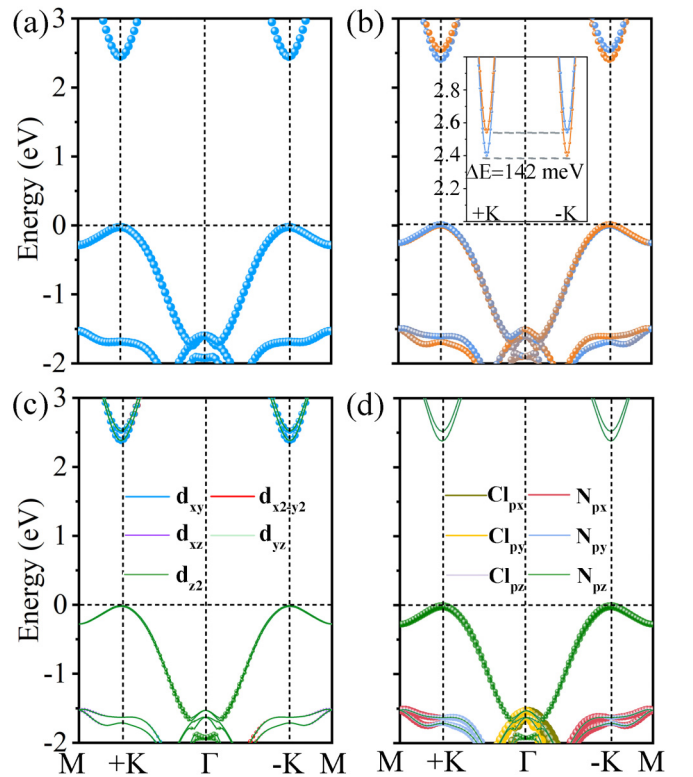

FIG. 2. Band structures of SL h-HfNCl (a) without and (b) with SOC based on the HSE06 functional. (c) d-orbital resolved band structure of SL h-HfNCl with SOC based on the HSE06 functional. (d) p-orbital resolved band structure of SL h-HfNCl with SOC based on the HSE06 functional. The Fermi level is set to 0 eV.

SL h-MNX, spin splitting occurs at the $+K$ and $-K$ valleys; see Figs. 2(b) and S3 [34]. However, for SL h-TiNBr, although it is an indirect gap semiconductor, its CBM locates at the $+K$ and $-K$ points, forming two valleys. To conveniently characterize the valley splitting in SL h-MNX, as shown in Fig. 1(d), we define $E_g = E^{C\downarrow}_{+K} - E^{V\downarrow}_{+K}$ as the band gap of valleys at the $+K(-K)$ points. ΔE_c and ΔE_v are, respectively, the valley splitting in the conduction and valence bands. The obtained values of the valley splitting for all these systems are summarized in Table I. Obviously, for all systems, the valley spin splitting in the conduction band is much larger than that in the valence band, which is distinct from that of TMDs wherein the valley spin splitting in the valence band is significantly larger than that in the conduction band [12,16]. Notably, the valley spin splitting in the conduction band in SL h-HfNCl and h-HfNBr even reach up to 142 and 162 meV, respectively, which are favorable for operating the valley index in experiment.

To understand the distinct discrepancy in the valley spin splitting between the valence and conduction bands, we employ the perturbation theory. It should be noted that all these systems hold similar electronic and valleytronic properties; we choose SL h-HfNCl as an example for explanation. Given that the valley spin splitting is induced by SOC, we therefore consider SOC as a perturbation. The effective Hamiltonian of the perturbation term for SL h-HfNCl can be given by

[50,51]

$$\hat{H}_{\text{SOC}} = \lambda \hat{L} \cdot \hat{S} = \hat{L}_z s_z + \hat{L}_+ s_- + \hat{L}_- s_+.$$

Here, $\hat{L}$ and $\hat{S}$ are the orbital angular moment and spin angular moment, respectively. From Figs. 2(c) and 2(d), and S4 in the Supplemental Material [34], we can see that the valleys in the conduction band are mainly contributed by Hf$-d_{x^2-y^2/xy}$ orbitals, while the valleys in the valence band are dominated by N$-p_z$ orbital. The basis functions thus can be chosen as

$$|\phi^\tau_c, \uparrow\rangle = \sqrt{\frac{1}{2}}(|d_{x^2-y^2}\rangle + i\tau|d_{xy}\rangle, \uparrow),$$

$$|\phi^\tau_c, \downarrow\rangle = \sqrt{\frac{1}{2}}(|d_{x^2-y^2}\rangle + i\tau|d_{xy}\rangle, \downarrow),$$

$$|\phi_v, \uparrow\rangle = |p_z, \uparrow\rangle,$$

$$|\phi_v, \downarrow\rangle = |p_z, \downarrow\rangle,$$

where ϕ^τ_c and ϕ_v are the wave functions of the conduction and valence bands at the $\pm K$ points, respectively. $\uparrow$ and $\downarrow$ represent spin-up and spin-down states, respectively. The superscript τ indicates the valley index ($\tau = \pm 1$). Under the influence of SOC, the variation of energy levels of $\pm K$ valley in the conduction band can be expressed as

$$E^{C\uparrow}_K = \langle \phi^1_c, \uparrow | \hat{H}_{\text{SOC}} | \phi^1_c, \uparrow \rangle = \tfrac{1}{2}(\langle d_{x^2-y^2} + id_{xy}, \uparrow | \hat{L}_z s_z | d_{x^2-y^2} + id_{xy}, \uparrow \rangle) > 0,$$

$$E^{C\downarrow}_K = \langle \phi^1_c, \downarrow | \hat{H}_{\text{SOC}} | \phi^1_c, \downarrow \rangle = \tfrac{1}{2}(\langle d_{x^2-y^2} + id_{xy}, \downarrow | \hat{L}_z s_z | d_{x^2-y^2} + id_{xy}, \downarrow \rangle) < 0,$$

$$E^{C\uparrow}_{-K} = \langle \phi^{-1}_c, \uparrow | \hat{H}_{\text{SOC}} | \phi^{-1}_c, \uparrow \rangle = \tfrac{1}{2}(\langle d_{x^2-y^2} - id_{xy}, \uparrow | \hat{L}_z s_z | d_{x^2-y^2} - id_{xy}, \uparrow \rangle) < 0,$$

$$E^{C\downarrow}_{-K} = \langle \phi^{-1}_c, \downarrow | \hat{H}_{\text{SOC}} | \phi^{-1}_c, \downarrow \rangle = \tfrac{1}{2}(\langle d_{x^2-y^2} - id_{xy}, \downarrow | \hat{L}_z s_z | d_{x^2-y^2} - id_{xy}, \downarrow \rangle) > 0.$$

Therefore, we obtain $\Delta E^C_K = E^{C\uparrow}_K - E^{C\downarrow}_K > 0$, $\Delta E^C_{-K} = E^{C\uparrow}_{-K} - E^{C\downarrow}_{-K} < 0$, which indicates that the valley spin splitting in the conduction band leads to opposite spin signs at the $+K$ and $-K$ valleys, while for the valence band, they can be expressed as

$$E^{V\uparrow}_K = E^{V\uparrow}_{-K} = \lambda\langle p_z, \uparrow | \hat{L}_z s_z | p_z, \uparrow \rangle + \langle p_z, \uparrow | \hat{L}_+ s_- | p_z, \uparrow \rangle + \langle p_z, \uparrow | \hat{L}_- s_+ | p_z, \uparrow \rangle = 0,$$

$$E^{V\downarrow}_K = E^{V\downarrow}_{-K} = \lambda\langle p_z, \downarrow | \hat{L}_z s_z | p_z, \downarrow \rangle + \langle p_z, \downarrow | \hat{L}_+ s_- | p_z, \downarrow \rangle + \langle p_z, \downarrow | \hat{L}_- s_+ | p_z, \downarrow \rangle = 0.$$

Accordingly, we can understand why the valley spin splitting in the conduction band of SL h-MNX is significantly larger than that in the valence band. A similar conclusion is also obtained based on ***k·p*** model analysis, which could be helpful for further discussion in the future work; see the Supplemental Material [34].

One can find that pristine SL h-MNX is not suitable for direct information storage, because the valleys are not polarized. In SL h-MNX, the broken inversion symmetry enables valley-dependent interplay of electrons with circularly polarized light, providing the opportunity to produce the valley polarization. We then analyze the optical selection rules in SL h-MNX. For the $+K$ and $-K$ valleys, they show a C_3

rotational symmetry. We also have $\hat{C}_3|\varphi_{v(c)}\rangle = e^{\frac{-i2\pi m_a}{3}}|\varphi_{v(c)}\rangle$ [52], where m_a is the magnetic quantum number; v and c denote the valleys in the valence and conduction bands, respectively. The right-hand (left-hand) circularly polarized light σ_+ (σ_-) can be described by $\hat{p}_\pm = \hat{p}_x \pm i\hat{p}_y$, where $\hat{p}$ indicates the momentum operator. When operating $\hat{C}_3$ on an eigenstate, we can get $C_3 \hat{p}_\pm C_3^{-1} = e^{\mp \frac{i2\pi}{3}} \hat{p}_\pm$. Under the circularly polarized light, the transition-matrix elements of the valleys in SL h-MNX can be expressed as

$$M_{cv} = \langle \varphi_c | \hat{p}_\pm | \varphi_v \rangle = \langle \varphi_c | C_3^{-1} C_3 \hat{p}_\pm C_3^{-1} C_3 | \varphi_v \rangle$$

$$= e^{-(m_c - m_v \pm 1)\frac{i2\pi}{3}} \langle \varphi_c | \hat{p}_\pm | \varphi_v \rangle.$$
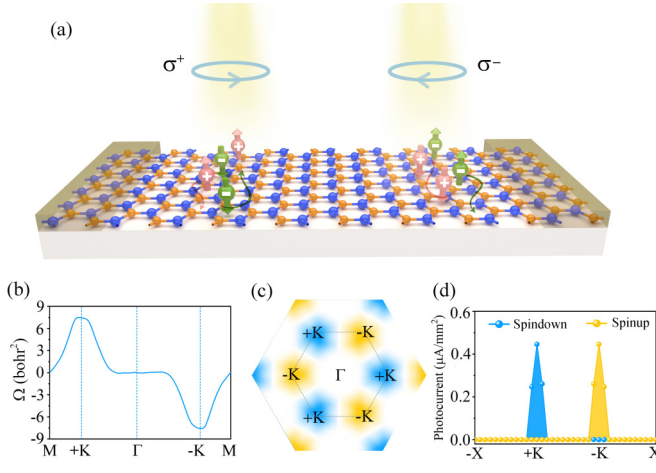
FIG. 3. (a) Schematic of valley polarization in devices with two probes. Arrows in (a) represent the movement directions of carriers in the presence of an in-plane electric field. (b) Berry curvature of SL h-HfNCl as a curve along the high-symmetry points. (c) Berry curvature of SL h-HfNCl as a contour map over the 2D BZ. (d) The calculated spin-polarized photocurrent of SL h-HfNCl along the high-symmetry points.

FIG. 4. Band structures of (a) layer 1-A with interlayer spacing of 2.13 Å and (b) layer 2-A with interlayer spacing of 2.40 Å. The variations of (c) valley splitting and (d) valley polarization with interlayer spacing in HfNCl/CrBr$_3$ heterostructures.

Obviously, if $m_c - m_v = \pm 2$, the above equation would be well defined. For $+K$ ($-K$) valleys, as $m_c = 2$ (-2) and $m_v = 0$ (0), the interband transitions thus can occur in the vicinity of $+K$ ($-K$) valleys under the right-hand (left-hand) circularly polarized light σ_+ (σ_-) with energy E_g.

To further validate the optical selection rule in SL h-MNX, taking SL h-HfNCl as an example, we investigate its photoresponse under circularly polarized light based on the density functional theory combined with Keldysh nonequilibrium Green's function (DFT-NEGF) method [53]. As shown in Fig. 3(a), we construct a two-probe model with a central scattering region sandwiched by two semi-infinite electrodes. Here, we define the transport direction along the armchair direction of SL h-HfNCl; the circularly polarized photon energy is equal to its energy gaps E_g. Due to the unit cell used in transport calculation being redefined as a rectangular one, the $+K$ ($-K$) point is folded; see Fig. S5 [34]. As shown in Figs. 3(d) and S6 [34], when carriers are excited by right-hand (left-hand) circularly polarized light, only the spin-down (spin-up) photocurrent is generated, manifesting the optical selection rules.

Since valley polarization is realized under circularly polarized light, we can expect the anomalous valley Hall effect in SL h-MNX, which is driven by the Berry curvature $\Omega(\vec{k})$. On the basis of the Kubo formula derivation [54], the Berry curvature is described by

$$\Omega(k) = -\sum_n \sum_{n \neq n'} f_n \frac{2\text{Im}\langle \psi_{nk}|v_x|\psi_{n'k}\rangle\langle \psi_{n'k}|v_y|\psi_{nk}\rangle}{(E_n - E_{n'})^2},$$

where f_n is the Fermi-Dirac distribution function, ψ_{nk} is the Bloch function and v_x (v_y) is the velocity operator along the x (y) direction. Figures 3(b) and 3(c) show the Berry curvatures of SL h-HfNCl as a curve along high-symmetry points and as a contour map in the whole 2D BZ, respectively. It can be seen
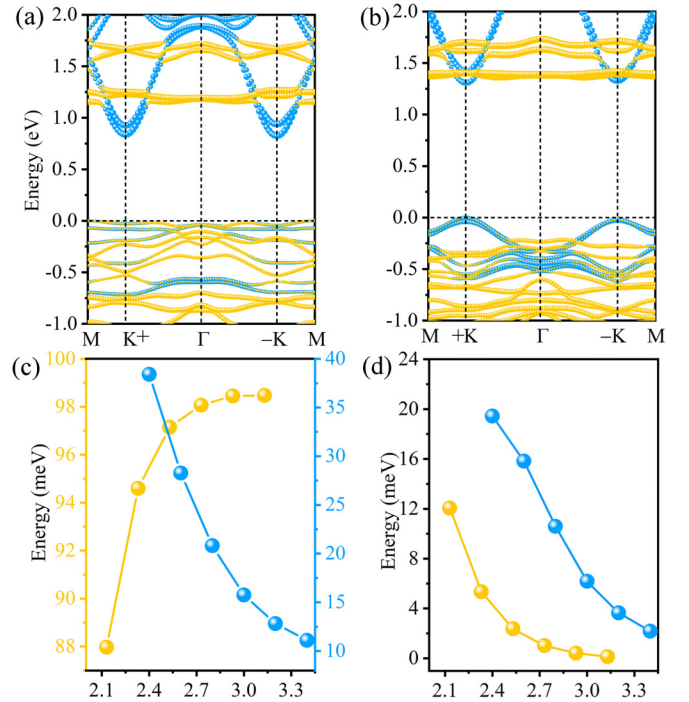
that the Berry curvature possesses nearly identical values, but takes opposite signs for the $+K$ and $-K$ valleys, suggesting the valley-contrasting character of SL h-HfNCl. Under the in-plane electric field, Bloch electrons will have an anomalous velocity of $\vec{v}_a \sim \vec{E} \times \Omega(\vec{k})$. The schematic of carrier movement in the circularly polarized light irradiated SL h-HfNCl in the presence of an in-plane electric field is shown in Fig. 3(a). When it is irradiated with right-hand polarized light with energy E_g, the excited spin-down electrons and spin-up holes from the $+K$ valley will accumulate in different boundaries of the sample with the help of an external electrical field, thus realizing the anomalous valley Hall effect. Due to the opposite sign of Berry curvature at the $-K$ valley, the excited electrons and holes under left-hand polarized light illumination exhibit contrary behaviors with respect to the $+K$ valley.

Aside from circularly polarized light, valley polarization in SL h-HfNCl can also be achieved when interfacing with ferromagnetic substrates. Here, we use SL CrBr$_3$, a well-known 2D ferromagnetic semiconductor, as the substrate to explore the valley polarization in SL h-HfNCl. A 2×2 supercell of SL h-HfNCl is adopted to match a unit cell of SL CrBr$_3$, which leads to a lattice mismatch of 1.8%. The interfacing of SL CrBr$_3$ with N- and Cl-terminated surfaces of SL h-HfNCl gives rise to two categories of heterostructures, which are named as layer 1 and layer 2, respectively. For the layer 1 (layer 2) structure, there are three typical stacking configurations: A, B, and C; see Fig. S7 [34]. Figure S8 [34] shows the band structures of HfNCl/CrBr$_3$ under these six configurations. Clearly, the valley polarization, on the order of meV, is realized in all these

systems; see Table S3 [34]. These values are comparable with that in WSe_2/CrI_3 heterostructures (~1 meV) [55], wherein the valley polarization has been observed in experiment [56,57].

Considering that the interlayer distance of a vdW heterostructure can be tuned via external approaches in experiment [58,59], the valley polarization in HfNCl/$CrBr_3$ is also expected to be tunable as it is strongly related to the interlayer coupling strength. Here, we choose the most stable configurations (layer 1-A and layer 2-A) to investigate the variation of valley polarization with the interlayer distance. As shown in Figs. 4(a) and 4(c), with decreasing interlayer distance, the valley splitting in the conduction band in configuration layer 1-A decreases, while the valley splitting in the valence band in configuration layer 2-A increases [Fig. 4(b)]. As expected, the valley polarizations in the conduction and valence bands gradually increase with decreasing interlayer distance [Fig. 4(d)], which can be attributed to the enhanced interaction between h-HfNCl and the ferromagnetic substrate. More importantly, the valley polarization in SL h-HfNCl can reach up to 20 meV, which is ten times larger than that of WSe_2/CrI_3 heterostructures.

Another interesting point we wish to address is the band alignment of the HfNCl/$CrBr_3$ heterostructure. When interfacing $CrBr_3$ with the N-terminated surface of h-HfNCl, the VBM of h-HfNCl is hybridized with the states from the substrate, while the valley characteristic in the conduction band is well preserved (Fig. S9 [34]), and thus the valley polarization occurs in the conduction band. In contrast, when interfacing $CrBr_3$ with the Cl-terminated surface of h-HfNCl, the CBM of h-HfNCl is submerged in the states from the substrate, while the valley characteristic in the valence band is well preserved. Such difference results from the huge difference in the electrostatic potentials of N- and Cl-terminated surfaces; see Fig. S10 [34]. Consequently, electron (hole) doping is required to detect the anomalous valley Hall effect in the layer 1(2)-A configurations.

III. CONCLUSION

To summarize, we propose a series of unique 2D valleytronic materials in SL h-MNX on the basis of first-principles calculations. SL h-MNX are found to be semiconductors with band gaps in the range 1.6–2.4 eV, which is a little bit larger than that of TMDs (0.8–2.0 eV). Significantly, due to the strong SOC strength, the CBM of SL h-MNX exhibits large valley spin splitting (38–162 meV), which is different from the cases of SL TMDs wherein the prominent valley spin splitting (145–450 meV) occurs in VBM. Also the carrier mobilities of SL h-MNX (~1800 cm^2 V^{-1} s^{-1}) are about an order of magnitude larger than that of TMDs (~200 cm^2 V^{-1} s^{-1}). These results strongly indicate that SL h-MNX provide excellent additions to the TMDs in valleytronics. Furthermore, the optical selection rules for the valley polarization in SL h-MNX are characterized in detail, and the pure valley and spin current can be obtained with circularly polarized light. The valley polarization is also achieved in SL h-HfNCl upon interfacing with $CrBr_3$. Interestingly, the valley polarization in HfNCl/$CrBr_3$ heterostructures is stacking dependent, and the valley polarization can be enhanced by decreasing the interlayer distance. Our work provides not only a series of unique 2D valleytronic materials but also efficient avenues to produce the valley polarization.

ACKNOWLEDGMENTS

[1] T. Norden, C. Zhao, P. Zhang, R. Sabirianov, A. Petrou, and H. Zeng, Nat. Commun. **10**, 4163 (2019).

[2] G. Liu, D. Xiao, Y. Yao, X. Xu, and W. Yao, Chem. Soc. Rev. **44**, 2643 (2015).

[3] J. Zhou, J. Lin, H. Sims, C. Jiang, C. Cong, J. Brehm, Z. Zhang, L. Niu, Y. Chen, Y. Zhou, Y. Wang, F. Liu, C. Zhu, W. Gao, Z. Liu, and W. Zhou, Adv. Mater. **32**, 1906536 (2020).

[4] C. Zhao, T. Norden, P. Zhang, P. Zhao, Y. Cheng, F. Sun, J. Parry, P. Taheri, J. Wang, Y. Yang, T. Scrace, K. Kang, S. Yang, G. Miao, R. Sabirianov, G. Kioseoglou, W. Huang, A. Petrou, and H. Zeng, Nat. Nanotechnol. **12**, 757 (2017).

[5] K. Mak, D. Xiao, and J. Shan, Nat. Photon. **12**, 451 (2018).

[6] Y. J. Zhang, T. Oka, R. Suzuki, J. T. Ye, and Y. Iwasa, Science **344**, 725 (2014).

[7] K. Mak, K. McGill, J. Park, and P. McEuen, Science **344**, 1489 (2014).

[8] J. Isberg, M. Gabrysch, J. Hammersberg, S. Majdi, K. K. Kovi, and D. J. Twitchen, Nat. Mater. **12**, 760 (2013).

[9] E. Barre, J. A. C. Incorvia, S. H. Kim, C. J. McClellan, E. Pop, H. S. P. Wong, and T. F. Heinz, Nano Lett. **19**, 770 (2019).

[10] D. Xiao, W. Yao, and Q. Niu, Phys. Rev. Lett. **99**, 236809 (2007).

[11] J. Mclver, B. Schulte, F. Stein, T. Matsuyama, G. Jotzu, G. Meier, and A. Cavalleri, Nat. Phys. **16**, 38 (2020).

[12] D. Xiao, G. Liu, W. Feng, X. Xu, and W. Yao, Phys. Rev. Lett. **108**, 196802 (2012).

[13] B. Zhu, H. Zeng, J. Dai, Z. Gong, and X. Cui, Proc. Natl Acad. Sci. USA **111**, 11606 (2014).

[14] C. Zhang, Y. Nie, S. Sanvito, and A. Du, Nano Lett. **19**, 1366 (2019).

[15] C. Ke, Y. Wu, W. Yang, Z. Wu, C. Zhang, X. Li, and J. Kang, Phys. Rev. B **100**, 195435 (2019).

[16] L. Xu, M. Yang, L. Shen, J. Zhou, T. Zhu, and Y. Feng, Phys. Rev. B **97**, 041405(R) (2018).

[17] W. Yao, D. Xiao, and Q. Niu, Phys. Rev. B **77**, 235406 (2008).

[18] T. Cao, G. Wang, W. Han, H. Ye, C. Zhu, J. Shi, Q. Niu, P. Tan, E. Wang, B. Liu, and J. Feng, Nat. Commun. **3**, 887 (2012).

[19] X. Zhang, Y. Lai, E. Dohner, S. Moon, T. Takashi, K. Watanabe, D. Smirnov, and T. Heinz, Phys. Rev. Lett. **122**, 127401 (2019).

[20] J. Qi, X. Li, Q. Niu, and J. Feng, Phys. Rev. B **92**, 121403(R) (2015).

[21] T. Zhou, J. Zhang, H. Jiang, L. Zutic, and Z. Yang, npj Quantun Mater. **3**, 39 (2018).

[22] Q. Zhang, S. Yang, W. Mi, Y. Cheng, and U. Schwingenschlögl, Adv. Mater. **28**, 7043 (2016).

[23] Q. Pei, B. Zhou, W. Mi, and Y. Cheng, ACS Appl. Mater. Inter. **11**, 12675 (2019).

[24] B. Zhai, J. Du, C. Shen, T. Wang, Y. Peng, Q. Zhang, and C. Xia, Phys. Rev. B **100**, 195307 (2019).

[25] X. Xu, Y. Ma, T. Zhang, C. Lei, B. Huang, and Y. Dai, J. Phys. Chem. Lett. **10**, 4535 (2019).

[26] N. Singh and U. Schwingenschlögl, Adv. Mater. **29**, 1600970 (2017).

[27] R. Peng, Y. Ma, S. Zhang, B. Huang, and Y. Dai, J. Phys. Chem. Lett. **9**, 3612 (2018).

[28] L. Yang, N. Sinitsyn, W. Chen, J. Yuan, J. Zhang, J. Lou, and S. Crooker, Nat. Phys. **11**, 830 (2015).

[29] J. Kim, C. Jin, B. Chen, H. Cai, T. Zhao, P. Lee, S. Kahn, K. Watanabe, T. Taniguchi, S. Tongay, M. Crommie, and F. Wang, Sci. Adv. **3**, e1700518 (2017).

[30] D. J. P. Sousa, M. Sammon, R. Kim, H. Li, I. Young, and T. Low, Phys. Rev. B **106**, 184412 (2022).

[31] W. Tong, S. Gong, X. Wan, and C. Duan, Nat. Commun. **7**, 13612 (2016).

[32] Y. Liu, Y. Gao, S. Zhang, J. He, and Z. Liu, Nano Res. **12**, 2695 (2019).

[33] J. Schaibley, H. Yu, G. Clark, P. Rivera, J. Ross, K. Seyler, W. Yao, and X. Xu, Nat. Rev. Mater. **1**, 16055 (2016).

[34] See Supplemental Material at http://link.aps.org/supplemental/10.1103/PhysRevB.107.035416 for the details of computational methods, carrier mobilities, and phonon dispersions of SL; and band AU: Check our changes to punctuation. It was not clear how to group the items.structures of SL and heterobilayers; also see Refs. [35–49].

[35] G. Kresse and J. Furthmüller, Comput. Mater. Sci. **6**, 15 (1996).

[36] G. Kresse and J. Furthmüller, Phys. Rev. B **54**, 11169 (1996).

[37] P. E. Blochl, Phys. Rev. B **50**, 17953 (1994).

[38] G. Kresse and D. Joubert, Phys. Rev. B **59**, 1758 (1999).

[39] J. Perdew, K. Burke, and M. Ernzerhof, Phys. Rev. Lett. **77**, 3865 (1996).

[40] J. Heyd, G. Scuseria, and M. Ernzerhof, J. Chem. Phys. **118**, 8207 (2003).

[41] A. Togo and I. Tanaka, Scr. Mater. **108**, 1 (2015).

[42] A. Mostofi, J. Yates, P. Pizzi, Y. Lee, I. Souza, D. Vanderbilt, and N. Marzari, Comput. Phys. Commun. **178**, 685 (2008).

[43] J. Taylor, H. Guo, and J. Wang, Phys. Rev. B **63**, 245407 (2001).

[44] D. Waldron, P. Haney, B. Larade, A. MacDonald, and H. Guo, Phys. Rev. Lett. **96**, 166804 (2006).

[45] L. Henrickson, J. Appl. Phys. **91**, 6273 (2002).

[46] J. Bardeen and W. Shockley, Phys. Rev. **80**, 72 (1950).

[47] K. Kaasbjerg, K. Thygesen, and A. Jauho, Phys. Rev. B **87**, 235312 (2013).

[48] X. Ma, X. Wu, H. Wang, and Y. Wang, J. Mater. Chem. A **6**, 2295 (2018).

[49] B. Radisavljevic, A. Radenovic, J. Brivio, V. Giacometti, and A. Kis, Nat. Nanotechnol. **6**, 147 (2011).

[50] G. Liu, W. Shan, Y. Yao, W. Yao, and D. Xiao, Phys. Rev. B **88**, 085433 (2013).

[51] A. Kormanyos, V. Zolyomi, N. Drummond, and G. Burkard, Phys. Rev. X **4**, 011034 (2014).

[52] X. Li, T. Cao, Q. Niu, J. Shi, and J. Feng, Proc. Natl Acad. Sci. USA **110**, 3738 (2013).

[53] L. Zhang, K. Gong, J. Chen, L. Liu, Y. Zhu, D. Xiao, and H. Guo, Phys. Rev. B **90**, 195428 (2014).

[54] D. Thouless, M. Kohmoto, M. Nightingale, and M. Nijs, Phys. Rev. Lett. **49**, 405 (1982).

[55] Z. Zhang, X. Ni, H. Huang, L. Hu, and F. Liu, Phys. Rev. B **99**, 115441 (2019).

[56] D. Zhong, K. Seyler, X. Linpeng, R. Cheng, N. Sivadas, B. Huang, E. Schmidgall, T. Taniguchi, K. Watanabe, M. McGuire, W. Yao, D. Xiao, K. Fu, and X. Xu, Sci. Adv. **3**, e1603113 (2017).

[57] K. Seyler, D. Zhong, B. Huang, X. Lipeng, N. Wilson, T. Taniguchi, K. Watanabe, W. Yao, D. Xiao, M. McGuire, K. Fu, and X. Xu, Nano Lett. **18**, 3823 (2018).

[58] S. Tongay, W. Fan, J. Kang, J. Park, U. Koldemir, J. Suh, D. Narang, K. Liu, J. Ji, J. Li, R. Sinclair, and J. Wu, Nano Lett. **14**, 3185 (2014).

[59] M. Yankowitz, K. Watanabe, T. Taniguchi, P. San-Jose, and B. Leroy, Nat. Commun. **7**, 13168 (2016).